

RESEARCH PAPER

On the Existence of "Maia variables"

F. Kahraman Aliçavuş,^{1,2} G. Handler,³ S. Chowdhury,³ E. Niemczura,⁴ R. Jayaraman,⁵ P. De Cat,⁶ D. Ozuyar,⁷ and F. Aliçavuş^{1,2}

¹Çanakkale Onsekiz Mart University, Science Faculty, Physics Department, 17100, Çanakkale, Türkiye

²Çanakkale Onsekiz Mart University, Astrophysics Research Center and Ulupınar Observatory, TR-17100, Çanakkale, Türkiye

³Nicolaus Copernicus Astronomical Center, Polish Academy of Sciences, Bartycka 18, PL-00-716 Warsaw, Poland

⁴University of Wrocław, Astronomical Institute, Kopernika 11, 51-622, Wrocław, Poland

⁵Department of Physics, and Kavli Institute for Astrophysics and Space Reserch, M.I.T., Cambridge, MA 02139, USA

⁶Royal Observatory of Belgium, Ringlaan 3, B-1180 Brussel, Belgium

⁷Ankara University, Faculty of Science, Dept. of Astronomy and Space Sciences, 06100, Tandogan, Ankara, Türkiye

Author for correspondence: F. Kahraman Aliçavuş & G. Handler, Email: filizkahraman01@gmail.com, gerald@camk.edu.pl .

(Received dd Mmm YYYY; revised dd Mmm YYYY; accepted dd Mmm YYYY; first published online 27 January 2024)

Abstract

There are different classes of pulsating stars in the H-R diagram. While many of those classes are undisputed, some remain a mystery such as the objects historically called “Maia variables.” Whereas the presence of such a class was suggested seven decades ago, no pulsational driving mechanism is known that could excite short-period oscillations in these late B to early A-type stars. Alternative hypotheses that would render the reports of variability of those stars erroneous have been proposed such as incorrect effective temperatures, binarity or rapid rotation, but no certain conclusions have been reached yet. Therefore the existence of these variables as a homogeneous class of pulsating star is still under discussion. Meanwhile, many new candidates of these variables have been claimed especially by using photometric observations of space telescopes. In this study, we examined 31 objects that are alleged members of this hypothetical group and carried out detailed spectroscopic and photometric analyses to test the proposed hypotheses for their cause of variability. The T_{eff} , $\log g$, $\nu \sin i$, and chemical abundances of the targets were determined and the *TESS* photometric data were examined. As a result, we found that most of these targets are located inside the δ Scuti, β Cephei or SPB star instability strips, a few show evidence for binarity and others for rapid rotation. We give arguments that none of the apparently rapid pulsations in our targets is caused by a star outside any known instability strip. By extrapolation, we argue that most stars proposed as pulsators outside well-established instability domains are misclassified. Hence there is no sufficient evidence justifying the existence of a class of pulsating stars formerly known as the “Maia variables.”

Keywords: stars: oscillations, stars: variables: general, techniques: photometric, techniques: spectroscopic

1. INTRODUCTION

Perhaps the most efficient and accurate way to investigate stellar interior structure is asteroseismology which uses the eigenfrequencies of stellar oscillations to probe the interiors of stars. Using asteroseismology phenomena such as internal rotation, angular momentum, and convective core overshooting have been successfully examined (e.g., Christophe et al., 2018; Townsend et al., 2018; Walczak et al., 2019; Kurtz, 2022).

The loci of several different classes of pulsating stars can be delineated in the Hertzsprung–Russell (H-R) diagram. These loci are called “instability strips” and comprise groups of different evolutionary statuses. Among those on the main sequence, six types of pulsating stars are commonly known. Moving from hotter to cooler temperatures, these variables are the β Cephei stars, the slowly pulsating B-type (SPB) stars, the δ Scuti stars, the rapidly oscillating Ap (roAp) stars, the γ Doradus stars and solar-like oscillators. The β Cephei stars are objects of spectral types B0 – B3 showing low-order pressure (p) and gravity (g) modes with frequencies $\gtrsim 3.5 \text{ d}^{-1}$ (Stankov & Handler, 2005). On the other hand, the SPB variables are B3 – B9 stars which exhibit high-order g-mode oscillations with frequencies $\lesssim 3.5 \text{ d}^{-1}$ (Aerts et al., 2010). The δ Scuti stars exhibit high-frequencies ($\gtrsim 5 \text{ d}^{-1}$) similar to β Cephei variables, however, their spectral types range from

A2 to F5 (Chang et al., 2013; Uytterhoeven et al., 2011). The roAp stars comprise similar spectral types, but are chemically peculiar due to the presence of strong magnetic fields and pulsate in high-order pressure modes with even higher frequencies ($\gtrsim 50 \text{ d}^{-1}$) (Holdsworth et al., 2024). The γ Doradus stars are low-frequency ($\lesssim 5 \text{ d}^{-1}$) g mode pulsators with spectral types of F2 – F6 (Uytterhoeven et al., 2011). Solar-like oscillators are of even later spectral type on the main sequence and show stochastic high-order p mode oscillations with frequencies around 300 d^{-1} (e.g., Jackiewicz, 2021). All these pulsators have their own instability strips where theoretical models can explain the observed types of oscillations. Consequently, almost the whole main sequence is populated with pulsating stars with spectral types ranging from early B to late G, but with a marked gap between spectral types B9 and A2. The reason for this gap is that both B-type variable star classes show pulsations triggered by the κ mechanism operating in the partial ionization zone of iron group elements (Dziembowski et al., 1993), but the δ Scuti stars are triggered by the κ and/or the turbulent mechanism acting in the partial ionization zones of Helium (Baker & Kippenhahn, 1962; Antoci et al., 2014) and hydrogen (e.g., Cunha et al., 2013). In the gap between those groups of pulsators at late B/early A spectral type, none of the currently known pulsation mechanisms is able to drive

pulsations in models, consistent with observations. In particular, no pulsations with intrinsic frequencies in excess of 3 d^{-1} should exist in stars with spectral types between B3 and A2.

However, a group of high-frequency pulsating stars in this gap and in the cool part of the SPB instability strip has been proposed by several authors (e.g., Struve, 1955; Lehmann et al., 1995). These variables seem to have high frequencies like β Cephei and δ Scuti stars but they are too cool to be a β Cephei and too hot to be a δ Scuti pulsator. Hence they appear to populate the gap where pressure mode pulsations should not exist. These variables have historically been known as the "Maia stars" following the apparent prototype of these variables, Maia in the Pleiades cluster. Maia was first thought to be a high-frequency pulsator (Struve, 1955), but this claim was refuted several times (e.g., McNamara, 1985, and references therein) and in the end it was shown that Maia is actually a rotational variable (HgMn star, White et al., 2017) without any detectable pulsational variability. However, recent studies, especially those based on space-based data, revived interest in those objects (Balona et al., 2016; Balona & Ozuyar, 2020; Balona, 2023).

Furthermore, examples of objects with slower apparently pulsational variations have been reported in the gap between the main sequence instability strips (e.g., Aerts & Kolenberg, 2005; Degroote et al., 2009; Mowlavi et al., 2013; Sharma et al., 2022), which are not to be confused with the short period variables mentioned above. Nevertheless, the hypotheses to explain all these variable stars are essentially the same. We call the first one the "rapid rotation hypothesis". This idea would explain the apparent pulsators as rapidly rotating SPB or β Cephei stars seen equator-on. Because of this fast rotation, the star would have an ellipsoidal-like shape, and its effective temperature (T_{eff}) would be lower near the equator and higher near the poles. This would have several consequences. First, the observationally determined T_{eff} would be different from the overall value due to projection effects, modifying the star's position in the HR Diagram. Second, the rapid rotation would shift the observed pulsational mode frequencies (Townsend, 2005; Salmon et al., 2014; Szweczek & Daszyńska-Daszkiewicz, 2017; Mowlavi et al., 2016) to higher values. Third, Rossby waves (r modes) could be excited (Szweczek & Daszyńska-Daszkiewicz, 2017; Saio et al., 2018). Fourth, the non-uniform temperature distribution in the star could facilitate pulsational excitation near the stellar poles or the equator (cf. Kurtz et al., 2023). Fifth, rapid rotation would extend the SPB instability strip, also towards lower temperatures (Townsend, 2005).

Another hypothesis to explain pulsation outside of any known instability strip is associated with binarity (hereinafter the "binary hypothesis"). The pulsating stars could be components of binary systems consisting of a non-pulsating late B-type star, which dominates the spectrum, and a δ Scuti pulsator. Given that most B-type stars have companions, and often more than one (Moe & Di Stefano, 2017), such a scenario is not unlikely. Therefore, apparent p-mode pulsations would be associated with a star too hot to have them excited. The third hypothesis involves simple observational uncertain-

ties that lead to incorrect T_{eff} values (hereinafter the "wrong T_{eff} hypothesis"). Most of the variables under question were observed by *Kepler* (Borucki et al., 2010) and the Transiting Exoplanet Survey Satellite (*TESS*, Ricker et al., 2014). The T_{eff} of these B type systems given in the *Kepler* and *TESS* input catalogues (Brown et al., 2011; Stassun et al., 2019) may not always be reliable. These T_{eff} parameters are in most cases photometric estimates based on a system lacking a U-band filter, and that carry some uncertainties regarding dereddening for stars located close to the Galactic plane (Stassun et al., 2019). Therefore the T_{eff} values for hot stars from the TIC catalogue have to be treated with caution. Finally, regarding *TESS* data, a "contamination hypothesis" must be considered. Due to the large (21") size of *TESS*'s CCD pixels on the sky, light of nearby stars may fall into the photometric aperture, hence, for the purpose of example, an unrelated δ Scuti star may introduce short-period pulsational variations into the light curve of a star outside of any pulsational instability strip.

Balona et al. (2016); Balona & Ozuyar (2020) tested some of these hypotheses, but without an adequate amount of good quality spectroscopic data. In a recent study Balona (2023) even suggested that Maia variables are an extension of δ Scuti stars and there is an interplay between available pulsational driving mechanisms, but this conclusion was partly based on inhomogeneous literature data. To improve on this situation one needs to study these variable stars with medium to high-resolution spectroscopic data to determine some important parameters (e.g. T_{eff} , rotational velocity) accurately.

In a recent study, Kurtz et al. (2023) analyzed a p-mode pulsator of spectral type A0 (HD 42477), which is located between the β Cephei and δ Scuti instability strips, to test the existence of p-mode oscillations in this region of H-R diagram by taking into account the incorrect T_{eff} , contamination, and binarity hypotheses. They ruled out or placed strong constraints against all these hypotheses and concluded that p-mode pulsations can be present in the mentioned region of the H-R diagram. Their excitation would be explained by coupling with g modes or by the classical $\kappa - \gamma$ mechanism operating in the HeII ionization zone in the stellar equatorial regions, hence is understood based on current astrophysical knowledge.

Recapitulating, there is one well-documented case of pressure mode pulsation between the instability strips of the SPB and δ Scuti stars. In addition, there are claims of hundreds of such stars based on space photometry data, but without proper assessments of whether the fast rotation, the binary, the contamination, or the wrong T_{eff} hypotheses would apply. Given the sheer number of these objects, is it really possible that most of them were claimed by misfortune?

In this study, we present detailed analyses of some candidate variables in the gap between the main sequence instability strips to test the proposed hypotheses and to establish whether a class of "Maia variables"^a is justified. We use *TESS* photometric data and medium and/or high-resolution spectra and

^aGiven that Maia itself is not a pulsating star, a different name for this prospective class would be required.

the paper is organized as follows. In Sect. 2, we introduce the target selection and observations. In Sect. 3, the spectroscopic analyses including radial velocity measurements, determination of atmospheric parameters, and chemical abundances are presented. A contamination analysis on *TESS* data is introduced in Sect. 4. Discussions and conclusions are given in Sect. 5, and 6, respectively.

2. Target selection and observations

Our variable star candidates were selected from the list of Balona & Ozuyar (2020). These authors defined priority classes considering the methods used to estimate T_{eff} values. The highest priority was given for spectroscopic T_{eff} while the lowest priority was defined for T_{eff} estimated from the spectral types. In between, there are T_{eff} estimations from some photometric colours. In this study, we preferentially chose stars of lower priority, as this adds more value to our spectral analyses for accurate T_{eff} determinations.

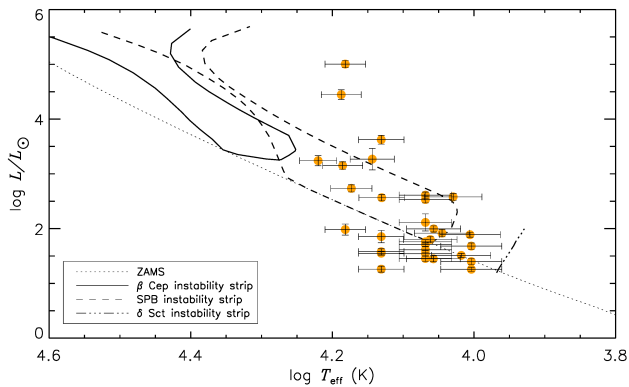


Figure 1. The initial positions of the selected candidates in the H-R diagram as derived by Balona & Ozuyar (2020). The theoretical instability strips of the β Cephei and SPB stars were taken from Pamyatnykh (1999). The domain of the δ Scuti stars was taken from Murphy et al. (2019).

We reanalyzed the *TESS* light curves of our selected candidates to confirm the presence of pressure mode oscillations in these variables. The data were analyzed using the Period04 (Lenz & Breger, 2005) package, which utilizes simultaneous multi-frequency sine-wave fitting with input parameter optimization. After removing the sine-wave fits from the original data, the residuals were then re-analyzed in the same manner to detect further periodicities. The signals were extracted until we reached a Signal-to-Noise ratio (SNR) of 4.5 (Baran & Koen, 2021). In addition, the initial positions of the selected candidates in the H-R diagram were checked using the luminosity (L) values calculated from the Gaia parallaxes (Gaia Collaboration, 2022), interstellar reddening, $E(B-V)$, calculated from the interstellar extinction map (Amôres & Lépine, 2005), the bolometric corrections (Flower, 1996) and the T_{eff} values given by Balona & Ozuyar (2020) (see, Fig. 1). As a result, 31 candidates were selected for this study; they are listed in Table 1.

For these candidates, we carried out spectroscopic surveys. Some spectra were taken from the Fibre-fed Échelle Spectro-

Table 1. The list of the targets. The number of the taken spectra from FIES and HERMES and their signal-to-noise ratios (SNR) are given in the last two columns, respectively. These spectra were taken between 2020 and 2021.

TIC	HD	V (mag)	#FIES/HERMES Spectra	SNR FIES/HERMES
16781787	207674	8.26	1/1	92 / 73
20534584	176052	8.41	-/2	- / 74, 78
26368855	222017	8.93	2/2	89, 38 / 70, 73
26369887	222142	9.55	1/1	49 / 53
27804376	210661	7.53	2/1	136, 65 / 103
36557487	49643	5.75	-/2	- / 123, 126
50850670		9.09	2/2	73, 49 / 30, 27
64774351	204905	7.24	3/2	138, 141, 140 / 96, 16
83803744	1009	8.38	2/-	71, 30 / -
90647390	278751	10.36	2/2	36, 29 / 13, 38
192780911	19921	7.73	1/2	145 / 56, 99
201739321	356	8.01	3/1	88, 24, 58 / 96
202567458	332044	9.87	2/-	67, 70 / -
236785664	175511	6.94	-/4	- / 86, 82, 141, 133
251196433		10.12	1/2	47 / 48, 45
255996252	196358	8.34	3/2	28, 59, 81 / 87, 86
312637783	228456	10.02	3/-	51, 56, 59 / -
317512446	220855	8.64	2/1	83, 74 / 15
335484421		8.73	2/-	100, 78 / -
352781227	351435	11.24	-/2	- / 23, 23
354793407	21699	5.46	-/2	- / 136, 112
367351021	216486	8.97	2/-	74, 80 / -
374038418		9.61	2/2	38, 34 / 48, 38
377099704	177195	8.74	-/5	- / 60, 66, 73, 70, 61
377443211	185757	8.31	2/1	62, 84 / 87
387757610	200506	8.13	2/2	89, 85 / 97, 20
402910080	193989	8.57	2/-	116, 108 / -
424032547	350990	10.32	2/-	52, 50 / -
434340780		9.14	2/-	89, 90 / -
450085823	287149	10.14	1/-	35 / -
467219052	239419	9.77	2/1	52, 40 / 63

graph (FIES, Telting *et al.*, 2014) that is a cross-dispersed high-resolution échelle spectrograph attached to the 2.56-m Nordic Optical Telescope of the Roque de los Muchachos Observatory (ORM, La Palma, Spain). It has three different resolution options; low ($R = 25000$), medium ($R = 46000$) and high ($R = 67000$). Considering the T_{eff} values and the V-band magnitudes of the target stars, the low-resolution mode was used during the observations to achieve a higher signal-to-noise ratio (SNR). In addition, this resolving power is good enough for spectral analysis of systems having medium to high projected rotational velocity ($\nu \sin i \gtrsim 30 \text{ km s}^{-1}$). We also gathered some spectra from the High Efficiency and Resolution Mercator Échelle Spectrograph (HERMES, Raskin *et al.*, 2011) which is a high-resolution ($R = 85000$) fibre-fed échelle spectrograph attached to the 1.2-m Mercator telescope at the Roque de los Muchachos Observatory (ORM, La Palma, Spain). Some stars have spectra from both spectrometers, while some have only from one. For each target, we tried to obtain at least two spectra taken at different times to check for possible binary-induced radial velocity shifts. The information about the spectroscopic surveys is given in Table 1.

3. Spectroscopic analysis

3.1 Radial velocity measurements

To discover possible variability of the targets induced by orbital motion in a binary system, we used spectra taken at different epochs. There are at least a few hours (mostly a day) or a maximum of around two months between two consecutive spectra of the same star for the same spectrometer.

The radial velocities of the systems were measured using the cross-correlation technique. The IRAF^b(Tody, 1986) FXCOR task was used in the investigation. As templates, some synthetic spectra were generated with different T_{eff} values of 8000 K, 10000 K and 15000 K. These atmospheric models were generated using local thermodynamic equilibrium (LTE) ATLAS9 models (Kurucz, 1993) and the SYNTH code (Kurucz & Avrett, 1981). Each spectrum of the individual stars was analyzed. However, for most of the stars, no trace of another component and no significant difference between the radial velocity measurements were found. There are two systems, TIC 202567458 and TIC 251196433, whose line profile shapes differ from those of single stars. However, because of high rotation and low SNR values, we could not detect double peaks in cross-correlation analyses of these systems. The line profile shapes of the two atypical systems could be caused by pulsations as well. We classified these systems as suspected binaries. Table A1 gives a list of the radial velocity measurements.

3.2 Atmospheric parameters

For the analysis of stars having T_{eff} lower than ~ 15000 K LTE model atmospheres are convenient (Przybilla *et al.*, 2011). Therefore at the beginning of our study, to estimate the T_{eff} , surface gravity ($\log g$), and $\nu \sin i$ parameters we used LTE ATLAS9 models (Kurucz, 1993) and SYNTH code (Kurucz &

Avrett, 1981) to generate theoretical spectra. The $\nu \sin i$ values were determined by the profile fitting method using unblended metal or helium (He) lines (Gray, 2008). The T_{eff} and $\log g$ parameters were derived utilizing the hydrogen lines. During the analysis, the minimization method was used to obtain the atmospheric parameters (Catanzaro *et al.*, 2004). Since most stars in our list seem to have moderate to high rotational velocity, rather than taking into account the resolving power of the spectrometers we preferred the spectra which have the highest SNR, if a star was observed by both spectrometers.

According to initially derived T_{eff} parameters from the LTE models, some stars were found hotter than 15000 K. For these stars, the same analysis was carried out by using the non-LTE TLUSTY BSTAR2006 grids (Lanz & Hubeny, 2007). These non-LTE models were generated using the Synspec (Hubeny & Lanz, 2011) program. As a result of LTE and non-LTE analyses, the estimated parameters are listed in Table 2. The uncertainties of the determined parameters were estimated by the $1-\sigma$ tolerance in the goodness-of-fit parameter. The consistency between the theoretical and observed spectra is shown in Fig. 2 for some samples.

3.3 Chemical abundances

After we determined the parameters given in Table 2, in the next step we singled out stars that are suitable for chemical abundance analysis. The stars having $\nu \sin i$ lower than $\sim 200 \text{ km s}^{-1}$, and spectra with a good SNR were chosen for that purpose. During this examination, previously derived atmospheric parameters were taken as input and they were updated utilizing the excitation and ionization equilibrium as described by Kahraman Aliçavuş *et al.* (2016).

In the analysis, the Kurucz line list^c was used for the line identification and we used the LTE ATLAS9 models. The spectral synthesis method was considered in the analysis. As a result of the investigation, updated atmospheric parameters and chemical abundances were derived. The list of the updated parameters is given in Table 2, while the element abundances are presented in Table A2. The distribution of the final T_{eff} , $\log g$, and $\nu \sin i$ parameters for all targets are shown in Fig. 3. In addition, the Fe abundance distribution of stars is shown in Fig. 4.

4. Examination of contamination

To complement our spectroscopic analyses, we used data from *TESS*. However, the *TESS* pixel scale is $21''$, which may induce contamination of the photometric signal from stars located nearby in the sky. To characterize the extent of the contamination in the *TESS* data of our candidates, we worked directly with target pixel files (TPFs).

For any star in which the contamination percentage was greater than 1%, we queried Gaia DR3 for all the stars brighter than a G_{mag} of 17 within a $200''$ radius of the *TESS* source. Any targets that had a star within the SPOC photometric aperture that had $\Delta G_{\text{mag}} < 5$ were thoroughly investigated

^b<http://iraf.noao.edu/>

^c<http://kurucz.harvard.edu/linelists.html>

Table 2. Atmospheric parameters of the stars determined from the hydrogen Balmer lines and the updated parameters. An asterisk represents a fixed $\log g$ value for TIC 352781227 that we could not determine because of rapid rotation and low SNR. Since some stars are not suitable for further analysis because of their large rotational velocities and low SNR values of their spectra, only some of the parameters could be updated (see, Sect 3.3). $E(B - V)$ was determined from the sodium lines and the final L parameters are given. The Gaia RUWE parameters are also listed in the last column.

TIC	Balmer lines		Updated Parameters				E(B-V) (mag \pm 0.02)	log L/L_{\odot}	RUWE
	T_{eff} (K)	log g (cgs)	T_{eff} (K)	log g (cgs)	ξ (km s $^{-1}$)	$\nu \sin i$ (km s $^{-1}$)			
16781787	11000 \pm 200	3.8 \pm 0.1				260 \pm 22	0.15	2.042 \pm 0.066	1.12
20534584	9600 \pm 200	3.6 \pm 0.1	9600 \pm 100	3.5 \pm 0.1	2.5 \pm 0.2	150 \pm 10	0.03	1.841 \pm 0.043	2.26
26368855	8500 \pm 100	4.0 \pm 0.1	8700 \pm 100	4.1 \pm 0.1	2.5 \pm 0.2	98 \pm 5	0.07	1.366 \pm 0.055	1.29
26369887	10000 \pm 500	3.5 \pm 0.1				230 \pm 10	0.05	1.469 \pm 0.055	0.99
27804376	8500 \pm 100	4.0 \pm 0.1	8800 \pm 100	4.0 \pm 0.1	1.5 \pm 0.2	135 \pm 10	0.07	1.288 \pm 0.054	1.15
36557487	14000 \pm 500	4.0 \pm 0.1				260 \pm 17	0.04	3.273 \pm 0.200	11.59
50850670	7400 \pm 100	4.0 \pm 0.1	7600 \pm 100	4.0 \pm 0.1	2.9 \pm 0.2	79 \pm 3	0.03	0.818 \pm 0.053	1.08
64774351	10000 \pm 200	4.0 \pm 0.1				230 \pm 14	0.01	1.867 \pm 0.050	0.89
83803744	12000 \pm 300	3.6 \pm 0.1	9800 \pm 200	4.0 \pm 0.1	2.5 \pm 0.2	21 \pm 4	0.25	2.443 \pm 0.057	1.13
90647390	7800 \pm 100	4.0 \pm 0.1	8100 \pm 200	4.1 \pm 0.1	2.8 \pm 0.2	42 \pm 4	0.18	1.384 \pm 0.101	4.25
192780911	12000 \pm 500	3.5 \pm 0.1				273 \pm 13	0.20	2.612 \pm 0.060	1.77
201739321	9000 \pm 100	4.0 \pm 0.1	9000 \pm 100	4.1 \pm 0.1	2.6 \pm 0.2	119 \pm 4	0.04	1.609 \pm 0.054	1.12
202567458	24000 \pm 1000	3.6 \pm 0.1				250 \pm 22	0.64	3.983 \pm 0.062	1.23
236785664	12500 \pm 500	4.0 \pm 0.1				260 \pm 20	0.02	2.579 \pm 0.058	1.20
251196433	19000 \pm 1000	3.5 \pm 0.1				255 \pm 15	0.15	2.590 \pm 0.087	2.01
255996252	8500 \pm 200	3.6 \pm 0.1	8600 \pm 100	3.9 \pm 0.1	3.6 \pm 0.2	98 \pm 5	0.02	1.233 \pm 0.055	0.91
312637783	21000 \pm 1000	3.8 \pm 0.2	22000 \pm 1000	3.5 \pm 0.2	1.5 \pm 0.2	19 \pm 2	0.40	3.725 \pm 0.091	3.53
317512446	9000 \pm 100	4.0 \pm 0.1	8900 \pm 100	4.1 \pm 0.1	3.0 \pm 0.2	40 \pm 2	0.05	1.363 \pm 0.053	0.94
335484421	7000 \pm 100	4.0 \pm 0.1	7300 \pm 100	4.0 \pm 0.1	3.2 \pm 0.2	56 \pm 3	0.03	1.170 \pm 0.054	0.93
352781227	9500 \pm 500	4.0*				\gtrsim 270	0.13	1.890 \pm 0.160	0.91
354793407	14000 \pm 1000	3.6 \pm 0.1	16000 \pm 1000	3.5 \pm 0.2	2.2 \pm 0.2	38 \pm 4	0.04	2.825 \pm 0.061	1.81
367351021	7700 \pm 100	4.0 \pm 0.1	7700 \pm 100	4.0 \pm 0.1	2.7 \pm 0.1	77 \pm 5	0.09	1.583 \pm 0.095	20.59
374038418	21000 \pm 1000	3.4 \pm 0.1	20000 \pm 1000	3.5 \pm 0.1	2.5 \pm 0.2	55 \pm 5	0.73	4.508 \pm 0.063	0.97
377099704	19000 \pm 1000	3.6 \pm 0.1	19000 \pm 1000	3.5 \pm 0.2	2.5 \pm 0.2	67 \pm 4	0.05	3.818 \pm 0.080	1.01
377443211	8500 \pm 100	4.0 \pm 0.1	8300 \pm 100	4.0 \pm 0.1	1.7 \pm 0.2	218 \pm 12	0.05	1.187 \pm 0.035	0.88
387757610	8200 \pm 200	4.0 \pm 0.1	8300 \pm 100	4.0 \pm 0.1	1.9 \pm 0.2	199 \pm 9	0.02	1.365 \pm 0.038	1.51
402910080	8500 \pm 200	3.5 \pm 0.1				270 \pm 25	0.00	1.487 \pm 0.032	0.99
424032547	14000 \pm 1000	3.5 \pm 0.1				270 \pm 27	0.02	2.724 \pm 0.063	0.88
434340780	9500 \pm 100	3.5 \pm 0.2				270 \pm 18	0.15	1.677 \pm 0.037	0.95
450085823	8500 \pm 300	4.0 \pm 0.2				100 \pm 16	0.17	1.267 \pm 0.037	0.99
467219052	8000 \pm 100	4.0 \pm 0.1	8100 \pm 100	4.0 \pm 0.1	3.1 \pm 0.1	111 \pm 7	0.30	1.879 \pm 0.055	0.94

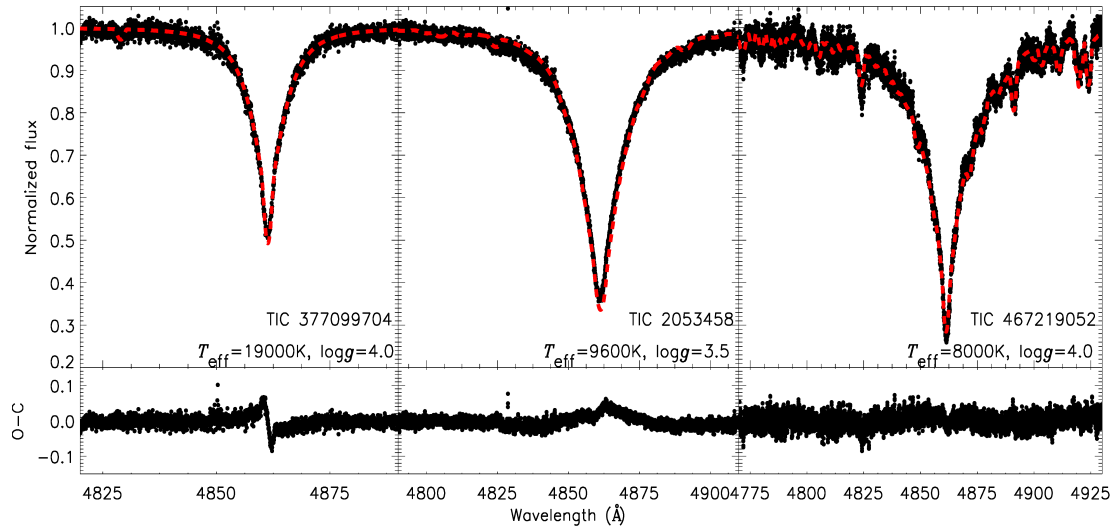


Figure 2. Upper panels: Theoretical spectral fits (red dashed lines) to the observed spectra of target stars. Lower panel: Residuals.

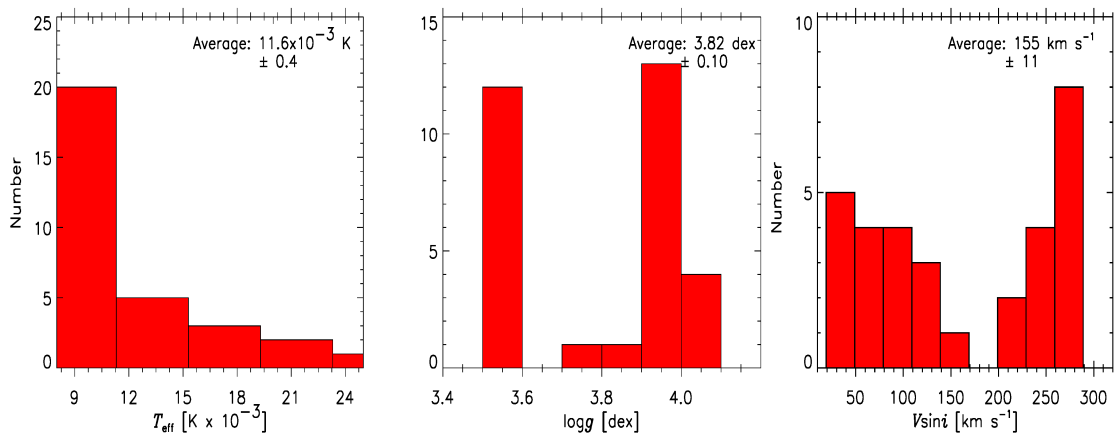


Figure 3. Distributions of the T_{eff} , $\log g$ and $v \sin i$ parameters.

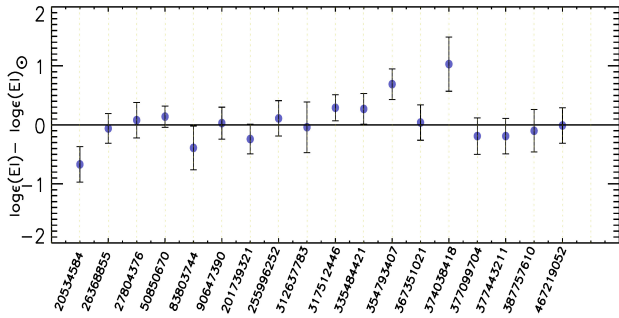


Figure 4. The differences between the obtained and solar (Asplund et al., 2009) Fe abundances for each star. The x-axis represents the TIC numbers.

through the use of custom apertures for photometry. We checked to see whether we recover the same periodicities for the Maia stars from the SPOC light curve and the light curve calculated using the custom aperture, which will allow us to have confidence in our identification of the pulsation modes.

As part of this analysis, 22 of the 31 stars were found to have contamination ratios greater than 1%. Several individual stars were selected for individual discussion in Appendix 1 if one of the following criteria was true: (i) There are changes in the number or location of significant frequencies when the periodogram of the custom light curve is calculated, (ii) there exist potentially contaminating stars that are within the SPOC photometric aperture and have a $\Delta G_{\text{mag}} \leq 3$ compared to the target of interest, or (iii) there is a star with $G_{\text{mag}} \leq 14$ whose signal falls into the same pixel as the star of interest. Some of the custom-generated light curves were corrected with cotrending basis vectors to remove long-term trends. The stars that are not discussed in Appendix 1 can be considered to have intrinsic variability that is appropriately reflected in the SPOC-generated light curves.

Note that there is a significant tradeoff between the custom light curves and the light curves generated by the SPOC pipeline—while the former will isolate signals to the star of interest, the white noise level will be somewhat higher because the detrending and photometry for this light curve are more rudimentary than the tools SPOC uses. This may mean that some of the lower S/N peaks in the periodogram for the SPOC light curve are washed out by the higher white noise level. Cases, where the white noise level of the custom light curve’s periodogram is comparable to the height of the peak in the periodogram of the SPOC light curve, are noted below.

Additionally, in some cases, we used the *TESS*-Localize package (Higgins & Bell, 2022) to identify the most likely source of some of the frequency peaks in the periodogram. All calls to *TESS*-Localize were used with the `principal_component` parameter set to 2, in order to de-trend the light curve generated from the TPF.

In Fig. 5, a plot of the *TESS* pixel files of TIC 64774351, TIC 352781227, TIC 467219052 and TIC 450085523 is presented. Custom apertures were created containing just the target stars. The periodograms for the custom apertures are shown in blue in the same figure. According to periodograms

and the discussion given in Appendix 1, for TIC 352781227, TIC 467219052, and TIC 450085523 we do not find any significant contamination that would cause frequencies higher than 3 d^{-1} . However, for TIC 64774351 the result of contamination analysis could not give a reliable result for high-frequencies seen in the original periodogram.

In Fig. 6, the heavily contaminated stars are shown. For TIC 255996252 according to our investigation, we found that the target of interest is the original source of high-frequencies (for detail see Appendix 1). However, for other systems, we were unable to distinguish whether the high-frequency peaks coming from our targets.

5. Discussion

We now proceed to the overall discussion of the variability of our sample of target stars. Each individual star is considered in more detail in Appendix 2. We present the positions of our targets in the theoretical H-R Diagram in Fig. 7.

The positions of the candidates in this diagram take into account the final atmospheric parameters, the structure of frequency spectra, and the $\nu \sin i$ values. To plot the final H-R diagram the L parameters were recalculated taking into account the final T_{eff} values. Additionally, the E(B-V) parameters were re-determined from the interstellar sodium lines as described in the study of Kahraman Aliçavuş et al. (2016) (cf. Table 2).

5.1 Incorrect T_{eff} hypothesis

In stark contrast to Fig. 1 most of the target stars now lie in known pulsational instability regions, suggesting that most literature T_{eff} values used to select them are inaccurate. We compared our spectral T_{eff} values with the T_{eff} of the TIC and Balona & Ozuyar (2020) in Fig. 8. As can be seen from the figure there are significant differences between the T_{eff} values. This result is an expected conclusion for the TIC T_{eff} values for hot stars because of the uncertain reddening corrections for stars in the Galactic plane. A similar explanation may apply to the T_{eff} values used by Balona & Ozuyar (2020), as those were derived mostly from photometric colours. According to this comparison, we conclude that for most targets previously derived T_{eff} values show significant discrepancies from the spectral ones. Even so, in Fig. 7 there are still some stars located outside of any known pulsational instability strip.

5.2 Binary hypothesis

According to the binary hypothesis, it was suggested that late B/early A type pressure mode pulsators could be binary systems including a B-type star with a δ Scuti companion. Hence, the system seems to be an oscillating star but it is too cool to be a δ Cephei and too hot to be a δ Scuti star. As a result of our investigation of the spectral line profiles and radial velocities of the stars in our sample, we did not reveal any obvious binary systems. Only two systems were classified as suspected binary systems because of their line profile changes, which however could be well caused by pulsations. Additionally, our method is not sensitive to binary systems with long orbital periods (more than a few months) given the temporal sampling of our

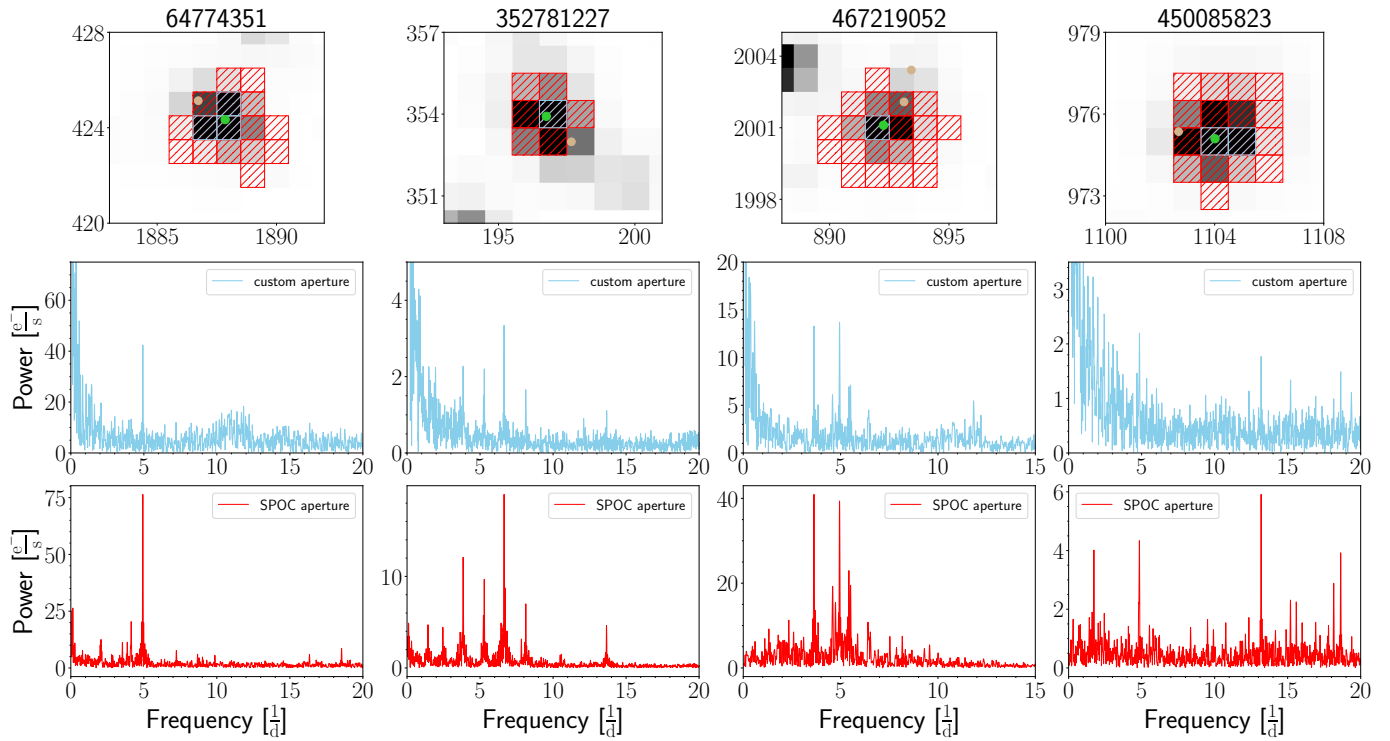


Figure 5. A plot of the *TESS* target pixel files of 4 of the 7 stars discussed in Appendix 1. These stars were the ones for which custom light curves were made. The top panel shows the target pixel files, with the star of interest shown in green (and indicated in the title) and the potentially contaminating stars shown in tan. The middle panel shows the light curve created using a custom aperture (shown in blue in the top panel); the bottom panel shows the light curve generated via the SPOC pipeline. Note that the y-axis scales differ between the middle and bottom panels as a result of the fact that the custom aperture imperfectly captures the flux from the star of interest. This, however, provides the advantage of allowing us to highlight the peak locations.

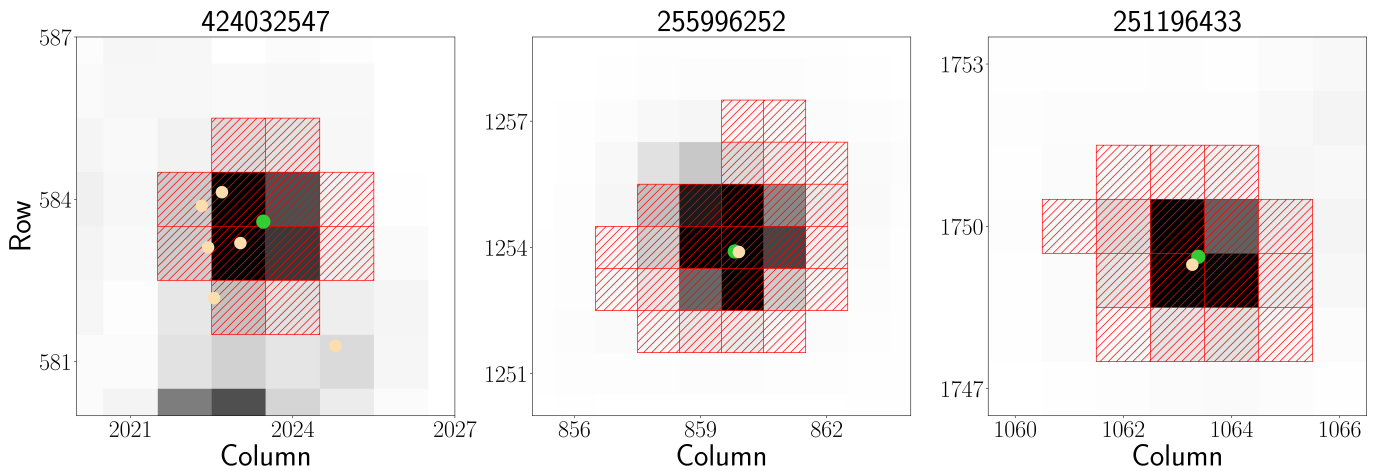


Figure 6. Each panel contains the target pixel file for a star that is so heavily contaminated that we are unable to determine where the true source of the frequency peaks in the periodogram lies. As in Figure 5, the green points represent the source of interest, while the tan points represent potentially contaminating stars.

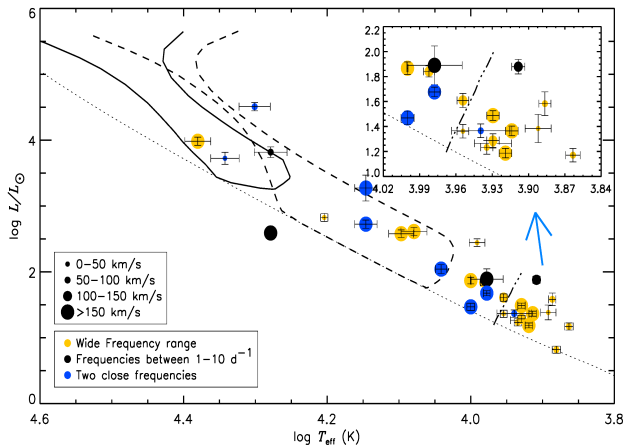


Figure 7. The final positions of the selected Maia candidates in the H-R diagram. The theoretical instability strips of β Cephei, SPB and δ Scuti stars were taken the same as in Fig. 1. A detailed explanation of the brief expressions of frequencies in the figure can be found in Sect. 5. Some targets are not included in this figure, since they were excluded from the Maia candidate list according to the results of our contamination analysis.

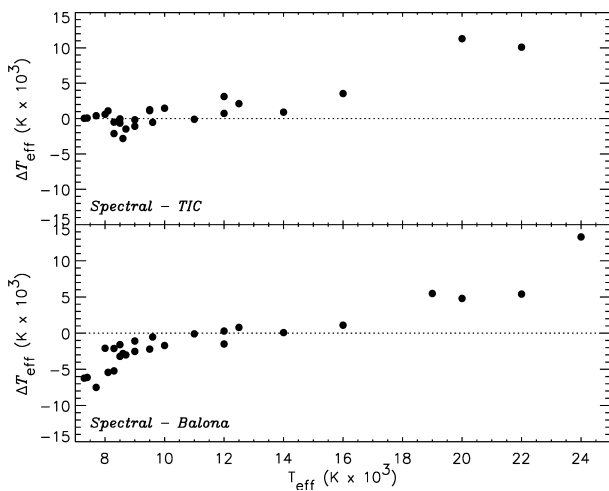


Figure 8. Comparison of the T_{eff} of the TIC (Stassun et al., 2019) (upper panel) and Balona & Ozuyar (2020) (lower panel) with the spectral T_{eff} determined in this study. The x-axis shows the spectral T_{eff} values while the y-axis illustrates the T_{eff} differences between the spectral and TIC (upper panel) and Balona & Ozuyar (2020) (lower panel).

spectra. Also, many stars in our sample show high rotational velocity ($>100 \text{ km s}^{-1}$) and some spectra have low SNR, which affects the radial velocity measurements and the detection of a possible binary component in the systems. Consequently, our spectroscopic investigation of possible binarity remained mostly inconclusive.

Another possibility to detect binaries would be to search for phase modulations of the pulsational signals (Murphy et al., 2014). Unfortunately, we were not able to find any evidence thereof, presumably owing to the small amplitudes of the pulsations detected and the relatively short duration of the individual *TESS* light curves.

We also examined the Gaia Renormalized Unit Weight Error (RUWE Lindegren et al. 2021). RUWE is a parameter that shows the degeneration in the astrometric parameters determined with Gaia (Gaia Collaboration et al., 2021). High values of RUWE (higher than 1.4) indicate that the system of interest could be a binary (Lindegren et al., 2018, 2021). Stassun & Torres (2021) also point out that any RUWE value above 1.0 may already be indicative of binarity. Therefore, we collected the RUWE parameters of our targets from Gaia DR3 (Gaia Collaboration et al., 2021) which are given in Table 2. As can be seen from the table, there are nine systems that have $\text{RUWE} > 1.4$. The largest values, 11.59 and 20.59, relate to TIC 36557487, and TIC 367351021, respectively. One suspected binary system from our radial velocity analysis (TIC 251196433) has a RUWE value of 2.01. The systems with high RUWE values (> 1.4) are likely astrometric binaries, even if none of our targets is in the list of non-single stars according to Gaia DR3.

5.3 Rapid rotation hypothesis

As discussed in the introduction, rapid rotation could a) modify star's position in the H-R Diagram, b) shift the observed pulsation frequencies, c) excite Rossby waves, and d) provide means of $\kappa - \gamma$ -driven excitation of p and g modes. To evaluate our candidate stars with respect to rotation we first took into account the stars which show frequencies between 1-10 d^{-1} . There are three stars that show frequencies in that range (TIC 352781227, TIC 377099704 and TIC 467219052) that are shown with black dots in Fig. 7. TIC 352781227 is placed between the δ Scuti and SPB instability strip. However, this variable exhibits high rotational velocity ($\gtrsim 270 \text{ km s}^{-1}$) which could cause low frequencies to be shifted towards high frequencies and since we likely see this star close to equator-on, our T_{eff} determination would be too low. Therefore, this variable is likely an SPB star. A more detailed discussion on this object is also given in Appendix 2. The other stars showing frequencies between 1-10 d^{-1} have low to moderate $v \sin i$. One is placed in the δ Scuti instability strip, while the other is located in the SPB domain, very close to the β Cephei territory (TIC 377099704). These stars are hence well placed in known instability strips. Both show both low and high frequencies, these stars could be SPB- β Cephei and a δ Scuti- γ Doradus hybrids.

There is a group of stars that are distinguished by two close frequencies dominant in the Fourier spectra (TIC 16781787,

TIC 26369887, TIC 36557487, TIC 312637783, TIC 374038418, TIC 434340780). As can be seen from Fig. 7 most of these stars rotate fast, and some of them are placed between the SPB and δ Scuti domains. Because of high rotational velocity, the rapidly rotating ones could appear cooler than they are and their pulsation frequencies could be shifted towards higher values. We therefore classify them as cool SPB stars. Also for these targets, more discussions are given in Appendix 2.

When we look at the other stars showing oscillations in a wide frequency range (up to 50 d^{-1}), we notice that most of them are located inside the δ Scuti instability strip. However, there are six of them placed beyond the hot border of δ Scuti instability strip. One of them, TIC 20534584, is placed in the area between the δ Scuti and SPB instability strips. It has moderate to high $\nu \sin i$ value (150 km s^{-1}) and we should keep in mind that the RUWE parameter of this system is 2.26. So the system could be a binary with a hotter component, hence we find the systems showing δ Scuti-type oscillation and over the hot border of δ Scuti instability strip. There are also four stars (TIC 83803744, TIC 192780911, TIC 236785664, TIC 354793407) placed inside the SPB domain and showing frequencies up to 40 d^{-1} . Two of these stars have low $\nu \sin i$ values, and while TIC 83803744 has a low RUWE parameter, TIC 354793407 has a RUWE of 1.81. For TIC 83803744 there is no hypotheses to explain the seen high frequencies. However, according to our examination (see Appendix 2) the system is known as HgMn star and often HgMn stars are found in binaries (e.g., Gerbaldi et al. 1985). Therefore TIC 83803744 likely is a binary system. The other two systems (TIC 192780911 and TIC 236785664) have large rotational velocities and their RUWE parameters are between around 1.8 and 1.2, respectively. Thus these systems could be binaries as well. TIC 192780911 exhibits a weak signal at around 3.9^{-1} , which could be an SPB-type pulsation modified by the rapid rotation of the star. TIC 236785664 show both low and high frequencies. Those high frequencies are typical for δ Scuti stars. However, the system is too hot to be a δ Scuti system. The last rapid rotator is TIC 202567458. This star's pulsation spectrum is composed of several apparent g-mode pulsations, linear combinations thereof, and of a stochastic component implying the presence of Internal Gravity Waves (IGWs, e.g., see Ratnasingam et al. 2023; Bowman et al. 2019). The higher frequency signals are explicable by combination frequencies.

5.4 Variability classification of the target stars

We summarize the discussions above and the results on the individual stars presented in Appendix 2 in Table 3, respectively. Out of the 31 stars considered in this paper and previously claimed as variables outside of any known instability strip, the largest group (14 objects) are normal δ Scuti stars that simply had overestimated T_{eff} . Six stars are gravity mode pulsators with combination frequencies that protrude into the pressure mode domain, but these higher frequencies are not due to independent pulsation modes (cf. Kurtz et al., 2015). Among the hottest stars, we found one star with gravity modes and Internal Gravity waves, two β Cephei pulsators, and two

β Cephei/SPB "hybrids".

Table 3. Variability classification of our target stars.

TIC	Variable type
16781787	SPB
20534584	g modes + comb. + δ Scuti
26368855	δ Scuti
26369887	SPB + combinations
27804376	δ Scuti
36557487	g modes + combinations
50850670	δ Scuti + γ Dor
64774351	g modes + combinations
83803744	ROT + δ Scuti binary?
90647390	δ Scuti + binary?
192780911	SPB + binary?
201739321	δ Scuti + ROT?
202567458	g modes + IGW
236785664	Be/SPB + δ Scuti ?
251196433	\checkmark 01chybrid \checkmark 201d β Cephei /SPB
255996252	δ Scuti
312637783	β Cephei + binary?
317512446	δ Scuti
335484421	δ Scuti
352781227	g modes + combinations
354793407	ROT + δ Scuti
367351021	δ Scuti + binary?
374038418	β Cephei + IGW
377099704	\checkmark 201chybrid \checkmark 201d β Cephei /SPB
377443211	δ Scuti
387757610	δ Scuti + γ Dor
402910080	δ Scuti
424032547	contamination
434340780	g modes + combinations
450085823	δ Scuti
467219052	δ Scuti

Regarding the remaining six objects, the *TESS* light curve of one target was revealed to be contaminated by a background ellipsoidal variable. Two stars were identified as SPB stars with a very fast rotation that presumably modifies the pulsation frequencies in the observer's reference frame to values that are comparable with those of pressure modes. That leaves three stars, two of which are in the SPB star instability strip and one is in between the SPB and the δ Scuti star domains. Two of these stars are rotational variables with additional frequencies in the δ Scuti range. For both of those, there is some indirect evidence of binarity, one has a RUWE of 1.81, and the other is a HgMn star which in most cases are binaries. Consequently, the short-period signals in these star's light curves might well arise from a δ Scuti companion. The last object is a rapidly rotating Be star with a somewhat high RUWE and several frequencies typical for δ Scuti stars. This latter object, TIC 236785664 = HD 175511, deserves some further investigation.

6. Conclusions

In this study, a detailed analysis of 31 stars that have been claimed as late B/early A type short period pulsators is presented. In this part of the H-R diagram no such pulsations are expected, so these objects need to be explained. There are four different hypotheses that are to be considered: incorrect T_{eff} , binarity, rapid rotation and a possible contamination of the light curves. To this end a detailed spectroscopic investigation was carried out for our candidate variables. For all stars accurate stellar parameters such as T_{eff} , $\log g$, $v \sin i$ were determined. Furthermore, individual element abundances were derived for all stars where this was possible. In addition, a contamination analysis was carried out to be sure that the determined high pulsation frequencies arise from the stars of interest.

There are several stars in our sample whose frequency spectra appear phenomenologically similar, hence we analysed them in groups. The first group shows a wide frequency range extending to $\sim 40 \text{ d}^{-1}$. Another group exhibits two dominant frequencies close to each other and the final group possesses frequencies between $1\text{--}10 \text{ d}^{-1}$. Taking into account these groups, the positions of the stars in the H-R diagram, $v \sin i$ values, the radial velocity measurements, and the RUWE parameter we discussed the proposed hypotheses on the existence of between the SPB and δ Scuti star instability strips. First, we conclude that incorrect T_{eff} values by themselves can not explain all of these stars even if for some systems there are significant differences between the spectroscopic and photometric T_{eff} values (see Fig. 8). The binary hypothesis alone is also insufficient. When we examined the high rotation hypothesis by considering the systems' positions in the H-R diagram and the structure of frequency spectra we identified some stars whose frequencies were likely shifted towards higher values due to rapid rotation.

However, taking into account a combination of all hypotheses, most of the 31 stars we studied can be explained easily. 27 are members of established variability classes, ranging from Internal Gravity Wave pulsators, β Cephei stars, SPB stars to δ Scuti and γ Dor stars. The variability of one object is due to a contaminating neighboring star. There are three stars that are not that easy to explain. Two of them are hot rotational variables which also exhibit short-period pulsations, but for both of them, we found indirect evidence for binarity. The last star is a rapidly rotating Be star in the SPB instability strip that also shows multiperiodic short-period pulsations, but also, in this case, the Gaia RUWE parameter is suspicious in terms of binarity.

Extrapolating our results to the hundreds of main sequence pulsators of B/A spectral type outside of any known instability region claimed recently (Balona, 2023), we expect that most if not all of these objects can be explained in different ways as well. From today's point of view, there is thus no need to claim the existence of an unexplained class of variable stars in this domain of the H-R diagram, let alone call them "Maia variables" as Maia itself is not a pulsating star (White et al., 2017).

Acknowledgement

This study has been supported by the Scientific and Technological Research Council (TUBITAK) project 121F474. GH thanks the Polish National Center for Science (NCN) for supporting the study through grants 2015/18/A/ST9/00578 and 2021/43/B/ST9/02972. Horizon 2020: (OPTICON) This project has received funding from the European Union's Horizon 2020 research and innovation programme under grant agreement No 730890. This material reflects only the authors views and the Commission is not liable for any use that may be made of the information contained therein. The calculations have been partly carried out using resources provided by the Wrocław Centre for Networking and Supercomputing (www.wcss.pl), Grant No 214. Based on observations made with the Mercator Telescope, operated on the island of La Palma by the Flemish Community, at the Spanish Observatorio del Roque de los Muchachos of the Instituto de Astrofísica de Canarias. The TESS data presented in this paper were obtained from the Mikulski Archive for Space Telescopes (MAST). Funding for the TESS mission is provided by the NASA Explorer Program. This work has made use of data from the European Space Agency (ESA) mission Gaia (<http://www.cosmos.esa.int/gaia>), processed by the Gaia Data Processing and Analysis Consortium (DPAC, <http://www.cosmos.esa.int/web/gaia/dpac/consortium>). Funding for the DPAC has been provided by national institutions, in particular, the institutions participating in the Gaia Multilateral Agreement. This research has made use of the SIMBAD database, operated at CDS, Strasbourg, France. We are grateful to Vichi Antoci, Tim Bedding, Dominic Bowman, Don Kurtz, Nami Mowlavi and Simon Murphy for their comments on a draft version of this paper.

References

- Aerts, C., Christensen-Dalsgaard, J., & Kurtz, D. W. 2010, *Asteroseismology*
- Aerts, C., & Kolenberg, K. 2005, *A&A*, 431, 615
- Amôres, E. B., & Lépine, J. R. D. 2005, *AJ*, 130, 659
- Antoci, V., Cunha, M., Houdek, G., et al. 2014, *ApJ*, 796, 118
- Asplund, M., Grevesse, N., Sauval, A. J., & Scott, P. 2009, *ARA&A*, 47, 481
- Baker, N., & Kippenhahn, R. 1962, *ZAp*, 54, 114
- Balona, L. A. 2023, *Frontiers in Astronomy and Space Sciences*, 10, 1266750
- Balona, L. A., & Ozuyar, D. 2020, *MNRAS*, 493, 5871
- Balona, L. A., Engelbrecht, C. A., Joshi, Y. C., et al. 2016, *MNRAS*, 460, 1318
- Baran, A. S., & Koen, C. 2021, *Acta Astron.*, 71, 113
- Borucki, W. J., Koch, D., Basri, G., et al. 2010, *Science*, 327, 977
- Bowman, D. M., Burssens, S., Pedersen, M. G., et al. 2019, *Nature Astronomy*, 3, 760
- Brown, T. M., Latham, D. W., Everett, M. E., & Esquerdo, G. A. 2011, *AJ*, 142, 112
- Catanzaro, G., Leone, F., & Dall, T. H. 2004, *A&A*, 425, 641
- Chang, S. W., Protopapas, P., Kim, D. W., & Byun, Y. I. 2013, *AJ*, 145, 132
- Charpinet, S., Brassard, P., Fontaine, G., et al. 2019, *A&A*, 632, A90
- Christophe, S., Ballot, J., Ouazzani, R. M., Antoci, V., & Salmon, S. J. A. J. 2018, *A&A*, 618, A47
- Cunha, M. S., Alentiev, D., Brandão, I. M., & Perraut, K. 2013, *MNRAS*, 436, 1639
- Degroote, P., Aerts, C., Ollivier, M., et al. 2009, *A&A*, 506, 471
- Dziembowski, W. A., Moskalik, P., & Pamyatnykh, A. A. 1993, *MNRAS*, 265, 588

- Flower, P. J. 1996, *ApJ*, 469, 355
- Gaia Collaboration. 2022, *VizieR Online Data Catalog*, I/355
- Gaia Collaboration, Smart, R. L., Sarro, L. M., et al. 2021, *A&A*, 649, A6
- Gerbaldi, M., Floquet, M., & Hauck, B. 1985, *A&A*, 146, 341
- Gray, D. F. 2008, *The Observation and Analysis of Stellar Photospheres*
- Higgins, M. E., & Bell, K. J. 2022, *TESS-Localize: Localize variable star signatures in TESS Photometry*, Astrophysics Source Code Library, record ascl:2204.005, ascl:2204.005
- Holdsworth, D. L., Cunha, M. S., Lares-Martiz, M., et al. 2024, *MNRAS*, 527, 9548
- Hubeny, I., & Lanz, T. 2011, *Synspec: General Spectrum Synthesis Program*, Astrophysics Source Code Library, record ascl:1109.022, ascl:1109.022
- Jackiewicz, J. 2021, *Frontiers in Astronomy and Space Sciences*, 7, 102
- Kahraman Aliçavuş, F., Niemczura, E., De Cat, P., et al. 2016, *MNRAS*, 458, 2307
- Kochukhov, O., Khalack, V., Kobzar, O., et al. 2021, *MNRAS*, 506, 5328
- Kurtz, D. W. 2022, *ARA&A*, 60, 31
- Kurtz, D. W., Jayaraman, R., Sowicka, P., et al. 2023, *MNRAS*, 521, 4765
- Kurtz, D. W., Shibahashi, H., Murphy, S. J., Bedding, T. R., & Bowman, D. M. 2015, *MNRAS*, 450, 3015
- Kurucz, R. 1993, *ATLAS9 Stellar Atmosphere Programs and 2 km/s grid*. Kurucz CD-ROM No. 13. Cambridge, 13
- Kurucz, R. L., & Avrett, E. H. 1981, *SAO Special Report*, 391
- Labadie-Bartz, J., Handler, G., Pepper, J., et al. 2020, *AJ*, 160, 32
- Lanz, T., & Hubeny, I. 2007, *ApJS*, 169, 83
- Lehmann, H., Scholz, G., Hildebrandt, G., et al. 1995, *A&A*, 300, 783
- Lenz, P., & Breger, M. 2005, *Communications in Asteroseismology*, 146, 53
- Lindegren, L., Hernández, J., Bombrun, A., et al. 2018, *A&A*, 616, A2
- Lindegren, L., Klioner, S. A., Hernández, J., et al. 2021, *A&A*, 649, A2
- McNamara, B. J. 1985, *ApJ*, 289, 213
- Moe, M., & Di Stefano, R. 2017, *ApJS*, 230, 15
- Mowlavi, N., Barblan, F., Saesen, S., & Eyer, L. 2013, *A&A*, 554, A108
- Mowlavi, N., Saesen, S., Semaan, T., et al. 2016, *A&A*, 595, L1
- Murphy, S. J., Bedding, T. R., Shibahashi, H., Kurtz, D. W., & Kjeldsen, H. 2014, *MNRAS*, 441, 2515
- Murphy, S. J., Hey, D., Van Reeth, T., & Bedding, T. R. 2019, *MNRAS*, 485, 2380
- Pamyatnykh, A. A. 1999, *Acta Astron.*, 49, 119
- Przybilla, N., Nieva, M.-F., & Butler, K. 2011, in *Journal of Physics Conference Series*, Vol. 328, *Journal of Physics Conference Series*, 012015
- Raskin, G., van Winckel, H., Hensberge, H., et al. 2011, *A&A*, 526, A69
- Ratnasingham, R. P., Rogers, T. M., Chowdhury, S., et al. 2023, *A&A*, 674, A134
- Ricker, G. R., Winn, J. N., Vanderspek, R., et al. 2014, in *Society of Photo-Optical Instrumentation Engineers (SPIE) Conference Series*, Vol. 9143, *Space Telescopes and Instrumentation 2014: Optical, Infrared, and Millimeter Wave*, ed. J. Oschmann, Jacobus M., M. Clampin, G. G. Fazio, & H. A. MacEwen, 914320
- Saio, H., Kurtz, D. W., Murphy, S. J., Antoci, V. L., & Lee, U. 2018, *MNRAS*, 474, 2774
- Salmon, S. J. A. J., Montalbán, J., Reese, D. R., Dupret, M. A., & Eggenberger, P. 2014, *A&A*, 569, A18
- Sharma, A. N., Bedding, T. R., Saio, H., & White, T. R. 2022, *MNRAS*, 515, 828
- Shore, S. N., Brown, D. N., & Sonneborn, G. 1987, *AJ*, 94, 737
- Stankov, A., & Handler, G. 2005, *ApJS*, 158, 193
- Stassun, K. G., & Torres, G. 2021, *ApJ*, 907, L33
- Stassun, K. G., Oelkers, R. J., Paegert, M., et al. 2019, *AJ*, 158, 138
- Struve, O. 1955, *S&T*, 14, 461
- Szewczuk, W., & Daszyńska-Daszkiewicz, J. 2017, *MNRAS*, 469, 13
- Telting, J. H., Avila, G., Buchhave, L., et al. 2014, *Astronomische Nachrichten*, 335, 41
- Tody, D. 1986, in *Society of Photo-Optical Instrumentation Engineers (SPIE) Conference Series*, Vol. 627, *Instrumentation in astronomy VI*, ed. D. L. Crawford, 733
- Townsend, R. H. D. 2005, *MNRAS*, 360, 465
- Townsend, R. H. D., Goldstein, J., & Zweibel, E. G. 2018, *MNRAS*, 475, 879
- Uytterhoeven, K., Moya, A., Grigahcène, A., et al. 2011, *A&A*, 534, A125
- Walczak, P., Daszyńska-Daszkiewicz, J., Pigulski, A., et al. 2019, *MNRAS*, 485, 3544
- White, T. R., Pope, B. J. S., Antoci, V., et al. 2017, *MNRAS*, 471, 2882

Appendix 1. Contamination analysis of individual stars

Appendix 1.1 TIC 64774351

The SPOC-derived light curve for TIC 64774351 has only 90.3% of its flux arising from the star of interest. There are two stars with $9 \leq G_{\text{mag}} \leq 10$ within $100''$ of TIC 64774351 (BD+52 2951 and BD+52 2952); the former is especially a key potential source of contamination. A light curve created from an aperture that does not include these two stars still shows a highly significant peak at 0.203 d, as shown in the left panel of Figure 5. However, some of the lower- and higher-frequency peaks (e.g., those around 4 d^{-1} and those between 15 and 20 d^{-1}) are not visible in the periodogram generated from the custom light curve. However, the white noise level is higher in the periodogram created from the custom aperture, which could hide these peaks, which are already relatively low signal-to-noise in the SPOC light curve. The nearby star, BD+52 2951 (indicated in tan in the top left panel of Figure 5), has a listed spectral type of F8, suggesting that it is likely not in the classical instability strip and should thus not pulsate.

An analysis of this star using the *TESS-Localize* tool suggests that the lower frequencies (those less than $\sim 5 \text{ d}^{-1}$) are highly likely to be associated with BD+52 2952. However, the analysis was unreliable for the higher frequencies (i.e., those greater than $\sim 5 \text{ d}^{-1}$), so in this case, we are unable to use *TESS-Localize* to draw any conclusions.

Appendix 1.2 TIC 251196433

The SPOC-derived light curve for this star has only 94.1% of its flux arising from the star of interest. There exists a star with $G_{\text{mag}} = 14$ within $4''$ (Gaia DR3 460981833479443456; henceforth referred to as GDR3-456); their locations in the TPF are shown in Figure 6. These two stars fall within the same pixel, making it nearly impossible to disentangle their respective variability via the use of custom apertures. Labadie-Bartz et al. (2020) identified TIC 251196433 as a β Cep star based on its low-frequency variability (most of the peaks are at frequencies less than 10 d^{-1}). However, this is also the regime of certain compact g mode pulsators.

Given that GDR3-456 has a similar parallax to TIC 251196433, they likely lie at similar distances, and so we can assume that the extinction coefficients (and thus, color excess) for both stars are roughly identical. Using the Gaia value of $E(G_{\text{BP}}-G_{\text{RP}})$ for TIC 251196433, we see that the color of GDR3-456 is around -0.17 , which could make it a cool sdB star. The pulsation amplitude is 0.7% for the highest amplitude frequency in the periodogram, which is too high for an sdB g mode pulsator and is thus likely associated with TIC 251196433. However, the

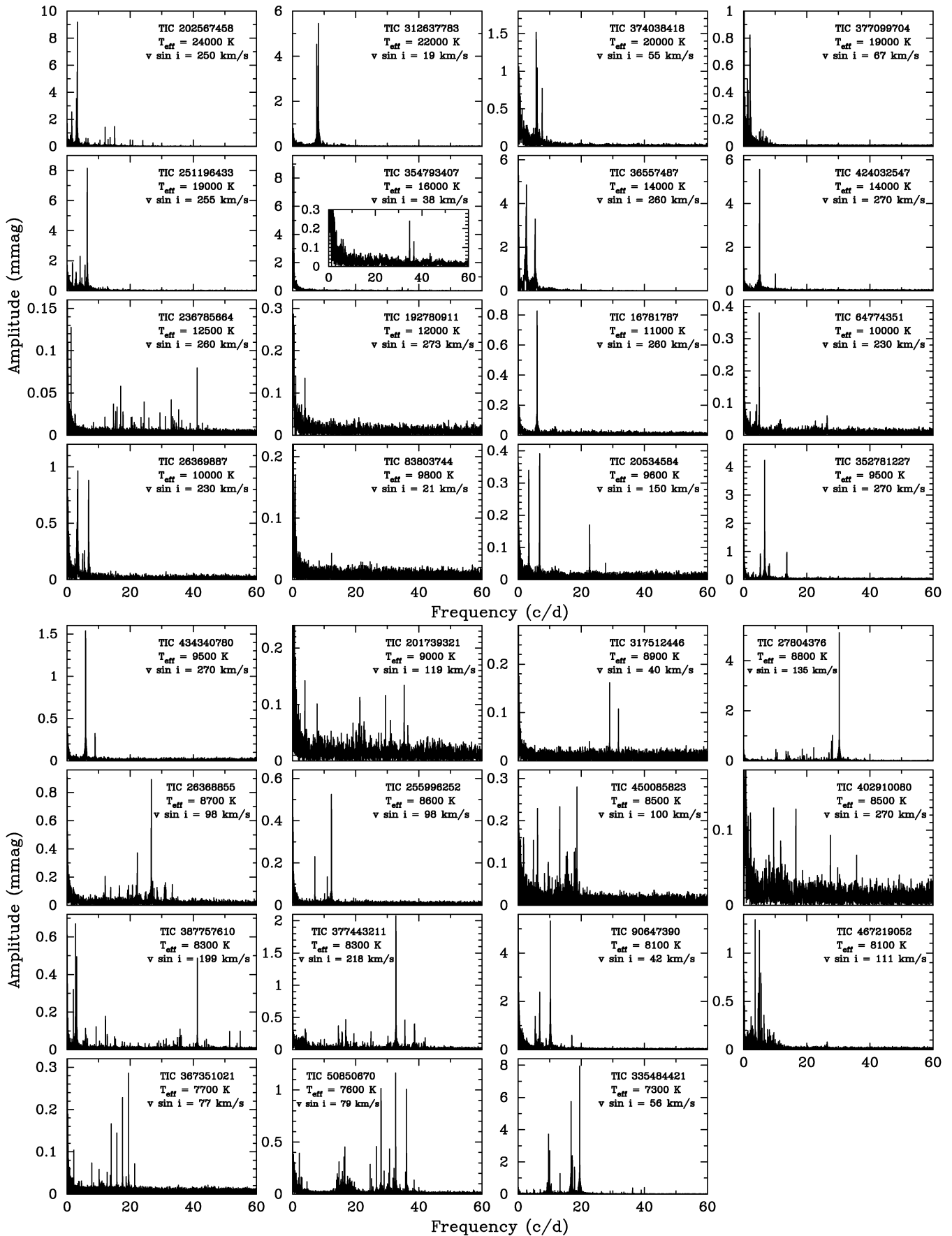


Figure A1. Amplitude spectra of the targets in order from the hottest star to the coldest star.

other peaks in the periodogram represent pulsation amplitudes of 0.15% or less; these modes could arise from the contaminating star GDR3-456.^d Further analyses, including speckle imaging and ground-based spectroscopy, may be needed to tease out the properties of this star and separate its modes from TIC 251196433.

Appendix 1.3 TIC 255996252

The SPOC light curve for this star has only 90.8% of its flux arising from the star of interest. As for TIC 251196433, and as shown in Figure 6, this star is nearly coincident in the sky with another star, Gaia DR3 2274443263522286208 ($G_{\text{mag}} = 12.49$; henceforth GDR3-208). This star is located at a similar distance as TIC 255996252, at around 210 pc based on parallax. GDR3-208, however, does not have any information about its color from Gaia DR3 or prior survey missions such as Hipparcos. Assuming similar extinctions A_G (a value is provided for this for TIC 255996252 in Gaia DR3), we get an absolute magnitude in G -band of 5.4, suggesting that it is likely a G -type star. Given that such stars' pulsation modes are convectively driven and exhibit clear frequency spacings, this star likely does not contaminate the light curve of TIC 255996252, and all the peaks seen in the star's Fourier spectrum can be taken to be intrinsic to this star.

Appendix 1.4 TIC 352781227

The SPOC light curve for this star has only 84.5% of the flux arising from TIC 352781227. This star has $G_{\text{mag}} = 11.28$, and there is a nearby star (within $30''$) with $G_{\text{mag}} = 12.82$. We created a custom aperture for the target pixel file containing just this star (shown in light blue shading in Figure 5, compared to the SPOC aperture in red shading). While this of course does not contain the entirety of the flux from this star (and so the peak amplitudes in the periodogram will be correspondingly lower), the periodogram should capture the frequencies of the peaks intrinsic to this star's variability. We find that the noise level of the periodogram is too high in the low-frequency regime ($\nu \lesssim 3 \text{ d}^{-1}$), so no conclusions can be drawn about these frequencies; however, the higher-frequency ones ($\nu \geq 3 \text{ d}^{-1}$) are very likely intrinsic to the star.

Appendix 1.5 TIC 424032547

Of all the stars in our sample, this star has the highest likelihood for contamination, as only 72.7% of the flux in the aperture comes from the star of interest. There is one significant peak at 5.03 d^{-1} , with at least 5 significant harmonics in the periodogram. An analysis of this TPF with *TESS*-Localize suggests that the probability that this frequency (and, by extension, its harmonics) is associated with that particular star is quite low. Indeed, as noted in Labadie-Bartz *et al.* (2020), this star is located in a dense region of an open cluster, such that the light curve and target pixel file suffer from significant

contamination and saturation that could affect the SPOC light curve.

Additional verification that the observed signal does not arise from this particular star lies in the VARIABLE flag assigned to stars in the Gaia catalog. There are two nearby stars (designated Gaia DR3 1823376830245623296 and DR3 1823376825919999232), which are somewhat fainter; however, both are designated with the VARIABLE flag in Gaia, while TIC 424032547 is not (its value for this flag is NOT_AVAILABLE). While this is not a sufficient condition to say that the observed variability does not arise from TIC 424032547, it is further strong evidence that suggests that the SPOC light curve does not capture the intrinsic variability for this star. The nearby contaminants are shown in the left panel of Figure 6.

Appendix 1.6 TIC 450085823

There is a nearby star with $G_{\text{mag}} = 14.04$, as shown in the rightmost panel of Figure 5. This star contributes 2.73% of the flux to the aperture used to construct the SPOC light curve, so it will likely have a minimal impact on the frequencies recovered from the light curve. We constructed a custom light curve using a two-pixel aperture and recovered most of the large amplitude peaks visible in the SPOC light curve, albeit at a lower S/N ratio. The peak at $\nu \sim 1.8 \text{ d}^{-1}$ is not visible in the custom light curve, perhaps due to the fact that it arises from the contaminating star. However, it could also simply be hidden below the noise. The high-frequency peaks are still visible in the custom light curve's analysis.

Appendix 1.7 TIC 467219052

This star has two potential nearby contaminants with Gaia magnitudes 12.06 and 12.94 (as seen in the third panel from left in Figure 5); the SPOC light curve captures 88% of the flux from the star of interest. A custom light curve from the single-pixel aperture shows that the largest peaks below 7 d^{-1} are likely intrinsic to this star. The peak at $\sim 11.8 \text{ d}^{-1}$ is significant in the custom light curve but is not present in the SPOC light curve. This may arise from some systematic variability in the custom light curve that was unable to be removed using the CBVs.

Further analysis using *TESS*-Localize provides some support to our conclusion that the lower frequencies arise from this star. The fits are not significant, but have $p < 0.2$, suggesting that this conclusion may be somewhat likely.

Appendix 2. Discussion of individual stars

Here we discuss each star according to their positions in the final H-R diagram, starting from the hottest objects and progressing towards lower T_{eff} . We give arguments about whether the given objects can be considered members of an established class of variable stars, or whether they cannot be explained this way.

^dFor an example of sdB stars pulsating in this regime, see Charpinet *et al.* (2019).

Appendix 2.1 Stars in the β Cephei domain

TIC 202567458 = HD 332044: the Fourier spectrum of this star's pulsations can be described by a basic multitude of signals between $1.48\text{--}1.56\text{ d}^{-1}$ as well as series of peaks at integer multiples thereof, extending up to 30 d^{-1} . In addition, there is a $1/f$ "noise floor" reminiscing the signals usually connected with Internal Gravity Waves (IGWs, e.g., see Ratnasingam et al. 2023). Given that the star lies close to the zero-age main sequence in Fig. 7, we conclude that the apparently coherent signals are due to gravity mode pulsations and their combination frequencies (Kurtz et al., 2015). Thus there is no reason for calling this object a "Maia" variable.

TIC 312637783 = HD 228456: this star shows multiple pulsation frequencies between $8\text{--}9\text{ d}^{-1}$ and 11 d^{-1} as well as some combination frequencies thereof. It has a high RUWE parameter of 3.53 (cf. Table 3.3). With this and the position of the star in Fig. 7, we classify this star as a suspected binary containing at least one β Cephei pulsator. There is nothing unusual about this object.

TIC 374038418 = BD+60 416: the Fourier spectrum is dominated by three coherent frequencies typical of β Cephei pulsators. Superposed on that is some non-coherent variability which could be due to IGWs or mass loss. All these phenomena are consistent with this object's temperature and luminosity put it in the β Cephei instability strip near the end of the main sequence phase. There is no need to invoke a possible "Maia" phenomenon.

TIC 377099704 = HD 177195: this star is located at the red edge of the β Cephei instability strip and inside the instability strip of the Slowly Pulsating B (SPB stars). Its pulsation spectrum is very complicated, with many modes in both the expected p and g mode frequency domains that do not seem to be harmonically related. We classify it as a "hybrid" β Cep/SPB pulsator.

TIC 251196433 = BD+57 655: this is a very rapidly rotating star with a large RUWE value suggestive of binarity. In Sect. 3.1 we also commented on its line-profile shape atypical of a single star. This object is located near the edges of both the β Cep and SPB instability strips. Its pulsation spectrum is dominated by an apparent p mode, and has many frequencies in both the β Cep and SPB domains plus some combination frequencies. According to us this is another "hybrid" β Cep/SPB pulsator.

Appendix 2.2 Stars in the SPB domain

TIC 354793407 = HD 21699: this star's light curve is dominated by a 2.5-d variation that is linked to rotation (Shore et al., 1987). Superposed on that is low-amplitude multiperiodic variability with periods around 40 minutes, typical for unevolved δ Scuti stars. At $T_{\text{eff}} = 16000\text{ K}$, this star is too hot to be a δ Scuti star (cf. Table 3.3). However, it also has a large RUWE of 1.81, suggestive of binarity. A hypothesized main sequence δ Scuti companion would be expected to have about 1/60 of the luminosity of the chemically peculiar primary. Therefore the small ($< 0.23\text{ mmag}$) short-period pulsation amplitudes in the *TESS* light curve would have intrinsic values of about 14

mmag and less, quite plausible for such an object. We therefore suspect that a binary companion is responsible for the short-period pulsations.

TIC 36557487 = HD 49643: similar to TIC 202567458, this star shows groups of closely spaced frequencies between 1.98 and 3.13 d^{-1} and harmonics thereof, extending out to 37 d^{-1} that we analogically classify as g mode pulsations. Apart from that, in *TESS* Sector 33 the light curve shows a sudden spectacular increase in total pulsation amplitude by a factor of about 15. Nevertheless, we find no reason why this object should be a "Maia" variable.

TIC 424032547 = HD 350990: the light curve of this object is dominated by a frequency of 5.025 d^{-1} whose amplitude is different within the three sectors it was observed. Interestingly, the amplitude of this variation is *inversely* correlated with the CROWDSAP parameter, i.e. the larger the flux contribution of the target in the photometric aperture, the lower the amplitude. This suggests that this object is not the source of the variability (cf. Sect. Appendix 1.5). Furthermore, careful prewhitening of the dominant frequency and its harmonics reveals the presence of a weak subharmonic. A phase fold of the light curve around the subharmonic frequency yields a light curve shape indicative of an ellipsoidal variable.

TIC 236785664 = HD 175511 is classified as a late-type Be star. The Fourier spectrum of its *TESS* light curve shows a single frequency near 1.24 d^{-1} and a multitude of peaks between 12 and 43 d^{-1} that are not harmonically related. Such pulsation frequencies would be typical for a δ Scuti star. At $T_{\text{eff}} = 12500\text{ K}$ this star is much hotter than such pulsators. Even its rapid rotation $\nu \sin i = 260\text{ km s}^{-1}$ should not create sufficient oblateness that its equatorial regions would be cool enough to excite pulsations. Only its Gaia RUWE parameter (1.20) gives a hint of possible binarity, which by itself we do not find sufficient to rule this object out as a "Maia" candidate.

TIC 192780911 = HD 19921: the *TESS* data show little intrinsic variability except for a weak signal at 3.9 d^{-1} , which could be an SPB-type pulsation modified by the rapid rotation of the star ($\nu \sin i = 273\text{ km s}^{-1}$). The RUWE value of 1.77 is suggestive of binarity.

TIC 16781787 = HD 207674: this object's variability is essentially singly periodic with a frequency of 6.0 d^{-1} . Two very weak signals near 2.35 d^{-1} are present in the S56 data, but are not subharmonics. As the strongest frequency is too high to be caused by rotation or binarity we speculate that this star's very rapid rotation shifts the dominant pulsation frequency to such a large value for an SPB star.

Appendix 2.3 Stars between the SPB and δ Scuti strips

TIC 64774351 = HD 204905: the frequency spectrum of this star changed between the Sector 15/16 and 56/57 observations, but the range of dominating frequencies remained around $4\text{--}5\text{ d}^{-1}$. The Fourier Transform contains peaks between $1\text{--}31\text{ d}^{-1}$ that do not appear to cluster in groups. However, a closer look reveals that the higher frequencies can in almost all cases be explained by combinations of lower frequencies. We therefore surmise that this star is related to those with

frequency groupings. The high frequency signals are then not intrinsic normal modes of pulsation but combination frequencies.

TIC 26369887 = HD 222142: there is a frequency group between $3.05\text{--}3.5\text{ d}^{-1}$ that, together with a single frequency of 2.47 d^{-1} , appears to form all other observed frequencies by linear combinations. This object then is a very cool SPB star. Its rapid rotation could have an influence on pulsational excitation. There are no high frequencies that would make this object a "Maia" candidate.

TIC 83803744 = HD 1009 is a HgMn star that has two periods consistently present in the *TESS* data sets, one at 0.89 d^{-1} that is apparently the first harmonic of its rotation period (Kochukhov *et al.*, 2021) and a low amplitude ($0.04 - 0.05$ mmag) apparent pulsation at 12.36 d^{-1} . Even though our two radial velocity measurements are consistent within the errors, it is known that HgMn stars often occur in binary systems (e.g., Gerbaldi *et al.* 1985) which is why we are reluctant to classify the apparent pulsation as "Maia" variability: the pulsations could arise from a δ Scuti companion.

TIC 20534584 = HD 176052: the low-frequency part of the Fourier Transform of the *TESS* light curve of this fairly rapid rotator ($v \sin i = 150\text{ km s}^{-1}$) is constituted by harmonically related frequencies based on a group around $3.35\text{--}3.40\text{ d}^{-1}$. A single significant higher frequency peak occurs at 22.64 d^{-1} with an amplitude of only 0.16 mmag. Given the high RUWE value of this object (2.26), we suspect that the high frequency variation comes from a companion of the δ Scuti type.

TIC 352781227 = HD 351435: this is a very rapid rotator with a consequently large uncertainty in its effective temperature (cf. Table 2). The pulsation spectra are clearly variable from sector to sector of data, but the underlying frequencies are the same. The frequencies themselves can be explained with groupings of combination frequencies of gravity mode pulsations.

TIC 434340780 = BD+61 2380 is a rapidly rotating star of Be spectral type. Its variability can be explained by a single gravity mode pulsation plus combination frequencies with higher amplitudes than the parent mode.

Appendix 2.4 Stars in the δ Scuti strip

The behaviour of all these objects is consistent with that of δ Scuti pulsators, which is also consistent with their positions in the HR Diagram. Nevertheless, they will be discussed briefly in what follows.

TIC 201739321 = HD 356 is located at the blue edge of the δ Scuti instability strip. The short-period variations can therefore be classified as δ Scuti pulsations. The two signals below 10 d^{-1} are harmonically related.

TIC 317512446 = HD 220855 is located just inside the δ Scuti instability strip. This is consistent with its two short-period pulsation frequencies.

TIC 27804376 = HD 210661 and TIC 26368855 = HD 222017 are two multiperiodic δ Scuti stars near the hot border of their pulsational instability strip with intermediate projected rotational velocities.

TIC 255996252 = HD 196358 has similar characteristics to the two stars just discussed, but its pulsation spectrum is not as rich.

TIC 450085823 = HD 287149 shows multiple pulsation frequencies of the δ Scuti type below 20 d^{-1} . Its pulsation spectrum exhibits considerable amplitude changes between its two *TESS* light curves taken two years apart.

TIC 402910080 = HD 193989 is a very rapidly rotating star with a wide range of δ Scuti type pulsation frequencies observed. Amplitude changes between the different epochs of *TESS* observations are easily discernable.

TIC 387757610 = HD 200506 is another rapidly rotating δ Scuti star. Its pulsation spectrum appears fairly stable over time and it also exhibits g mode pulsations of the γ Doradus type plus combination frequencies thereof.

TIC 377443211 = HD 185757 also rotates rapidly. It shows a wide range of δ Scuti type pulsation frequencies whose amplitudes somewhat change over time.

TIC 90647390 = HD 278751 shows a few δ Scuti type pulsations and some combination frequencies thereof. Its Gaia RUWE value strongly suggests binarity.

TIC 467219052 = HD 239419 is the slowest pulsating δ Scuti star in our sample, and it is also farthest away from the zero-age main sequence. Its pulsation amplitudes vary somewhat over time.

TIC 367351021 = HD 216486 has the highest RUWE value among our targets and a set of almost equally spaced δ Scuti type pulsation frequencies.

TIC 50850670 = BD+65 291 belongs to the δ Scuti stars of intermediate rotational velocities. It has three distinct groups of pulsation frequencies, the lowest frequency group likely due to γ Doradus type pulsations. The two other groups are separated by a factor of two in frequency but the individual modes are not harmonically related.

TIC 335484421 = BD+62 2044 is the coolest δ Scuti star in our sample, with a wide range and a large number of pulsation frequencies.

Table A1. Radial velocity measurements. * represents the cannot measure radial velocity value due to low signal-to-noise level.

TIC	FIES		HERMES	
	JD 2458000+	v_r (km/s)	JD 2459000+	v_r (km/s)
16781787	1122.4625	7.33 ± 2.52	1057.6369	3.44 ± 1.46
20534584			996.4778	-13.68 ± 2.22
			993.5008	-14.38 ± 2.15
			996.4778	-13.2 ± 2.53
26368855	1112.5543	-13.98 ± 2.56	1054.7315	-6.06 ± 1.35
	1112.4515	-6.81 ± 2.80	1056.7014	-6.40 ± 1.32
26369887	1112.5438	-2.02 ± 0.65	1057.7031	-1.36 ± 0.85
27804376	1120.3924	-9.30 ± 1.69	1052.6768	-17.65 ± 1.85
	1137.5354	-11.50 ± 2.16		
36557487			1190.6814	17.95 ± 2.53
			1190.6814	19.86 ± 2.86
50850670	1123.6194	-12.80 ± 1.86	1230.4578	5.41 ± 1.85
	1152.5264	-9.50 ± 1.33	1237.4024	4.67 ± 2.74
64774351	1121.4633	-9.03 ± 2.18	780.5811	-9.95 ± 2.37
		-4.21 ± 1.20	1083.6384	-9.50 ± 3.85
		-5.48 ± 1.28		
83803744	1112.5647	-14.19 ± 2.93		
	1113.6432	-14.00 ± 3.71		
90647390	1123.6362	-50.00 ± 3.41	1245.4465	-32.57 ± 4.27
	1152.5466	-38.72 ± 3.52	*	
192780911	1130.6064	-14.39 ± 2.45	1164.5964	0.15 ± 2.80
			1194.5904	2.44 ± 2.04
201739321	1112.5710	-20.78 ± 3.11	1056.7346	-9.75 ± 3.21
	1112.4675	-21.48 ± 4.83		
	1113.6515	-20.78 ± 3.11		
202567458				
236785664			625.4982	-15.50 ± 2.56
			660.5974	-4.41 ± 1.22
			990.4414	-7.01 ± 1.32
			991.4537	-6.98 ± 1.11
251196433	1153.4524	-30.18 ± 3.18	1147.6737	-33.63 ± 3.89
			1194.4703	-30.51 ± 3.69
255996252	1114.4288	7.47 ± 2.15	997.7101	9.39 ± 1.26
	1120.3858	8.04 ± 1.28	997.7101	10.70 ± 1.36
	1122.4441	7.04 ± 1.84		
312637783	1121.4469	11.62 ± 2.10		
	1122.4149	8.42 ± 1.83		
	1121.7385	5.68 ± 1.38		
317512446	1107.5420	9.40 ± 2.22		
	1107.6184	9.86 ± 1.78		
	1083.6451	3.04 ± 3.52		

Table A1. Continuation.

TIC	FIES		HERMES	
	JD 2458000+	v_r (km/s)	JD 2459000+	v_r (km/s)
335484421	1113.4823	0.26 ± 1.02		
	1123.3351	0.77 ± 0.98		
352781227			1056.5846	25.77 ± 5.32
			1056.6060	31.85 ± 5.58
354793407	1131.4274	-26.78 ± 2.15	1191.4345	4.77 ± 1.58
	1121.5663	-24.13 ± 2.27	1194.5965	5.29 ± 1.62
367351021	1120.3990	-60.00 ± 5.75	1260.4277	-63.91 ± 5.79
	1152.5566	-63.71 ± 5.79		
374038418	1120.3990	-60.00 ± 5.75	1260.4277	-63.91 ± 5.79
	1152.5566	-63.71 ± 5.79		
	1242.3445	-41.71 ± 5.14		
377099704			652.4951	-28.85 ± 2.18
			654.4107	-28.34 ± 2.08
			668.4067	-29.56 ± 1.85
			990.4497	-30.78 ± 1.98
			991.4639	-27.11 ± 2.31
377443211	1114.4406	-6.31 ± 1.89	997.7053	-18.21 ± 4.89
	1122.3990	-8.88 ± 2.50		
387757610	1119.3948	-16.81 ± 2.80	997.7178	-14.00 ± 2.41
	1122.4504	-14.48 ± 2.86	1083.6543	-10.24 ± 5.12
402910080	1119.3948	22.98 ± 4.17		
	1122.4344	16.76 ± 5.41		
424032547	1122.4045	13.06 ± 3.75		
	1138.4108	14.38 ± 4.20		
434340780	1120.3760	-7.39 ± 4.81		
	1153.3448	-3.75 ± 5.13		
450085823	1112.7434	10.25 ± 5.75		
467219052	1113.4962	1.68 ± 1.12	1056.6205	4.17 ± 2.15

Table A2. The result of the analysis of chemical abundances. The numbers given in the brackets represent the number of used lines in the analysis.

	TIC 20534584	_TIC 26368855_	_TIC 27804376_	_TIC 50850670_	_TIC 83803744_	_TIC 90647390_
Element	Abundance	Abundance	Abundance	Abundance	Abundance	Abundance
⁶ C		8.15 ± 0.33 (2)	8.41 ± 0.23 (6)			8.58 ± 0.29 (4)
⁷ N						
⁸ O		8.98 ± 0.33 (2)				
¹¹ Na			6.45 ± 0.42 (1)	6.47 ± 0.26 (2)		
¹² Mg	7.75 ± 0.46 (2)	7.88 ± 0.33 (2)	7.94 ± 0.52 (5)	8.02 ± 0.39 (4)	6.53 ± 0.31 (1)	7.93 ± 0.27 (4)
¹⁴ Si	7.26 ± 0.46 (2)	7.62 ± 0.37 (3)	7.30 ± 0.53 (4)	7.02 ± 0.36 (18)	7.85 ± 0.29 (2)	7.17 ± 0.37 (3)
¹⁶ S				7.39 ± 0.28 (2)		7.06 ± 0.34 (1)
²⁰ Ca	6.86 ± 0.45 (2)	6.43 ± 0.43 (13)	6.79 ± 0.47 (8)	5.86 ± 0.27 (15)	6.53 ± 0.30 (2)	6.71 ± 0.23 (8)
²¹ Sc	3.69 ± 0.45 (2)	3.19 ± 0.36 (3)	3.22 ± 0.35 (3)	2.58 ± 0.33 (5)	3.28 ± 0.33 (2)	3.27 ± 0.26 (2)
²² Ti	4.17 ± 0.36 (7)	4.97 ± 0.40 (17)	5.19 ± 0.38 (12)	4.72 ± 0.25 (34)	4.53 ± 0.26 (5)	5.31 ± 0.24 (18)
²³ V			4.44 ± 0.22 (2)	4.85 ± 0.33 (6)	5.00 ± 0.34 (2)	
²⁴ Cr	5.10 ± 0.36 (6)	5.80 ± 0.31 (10)	5.84 ± 0.25 (12)	5.69 ± 0.25 (33)	6.19 ± 0.27 (11)	6.01 ± 0.29 (10)
²⁵ Mn				5.45 ± 0.33 (10)	7.32 ± 0.35 (2)	6.31 ± 0.35 (2)
²⁶ Fe	6.83 ± 0.34 (15)	7.44 ± 0.25 (33)	7.58 ± 0.35 (42)	7.64 ± 0.18 (104)	7.11 ± 0.37 (14)	7.53 ± 0.27 (62)
²⁷ Co				5.72 ± 0.26 (2)		
²⁸ Ni		6.27 ± 0.34 (5)	6.24 ± 0.44 (11)	6.61 ± 0.21 (33)	5.86 ± 0.36 (1)	6.30 ± 0.30 (4)
²⁹ Cu				4.38 ± 0.27 (1)		
³⁰ Zn				4.43 ± 0.26 (1)		
³⁸ Sr		2.76 ± 0.33 (1)		3.39 ± 0.26 (2)	2.44 ± 0.32 (1)	
³⁹ Y	3.06 ± 0.46 (1)	2.45 ± 0.33 (2)	2.43 ± 0.42 (2)	2.67 ± 0.31 (6)	3.39 ± 0.36 (1)	2.24 ± 0.31 (2)
⁴⁰ Zr			2.89 ± 0.42 (1)	2.96 ± 0.26 (4)		
⁵⁶ Ba		2.14 ± 0.33 (2)	3.10 ± 0.42 (1)			2.61 ± 0.33 (2)

Table A2. Continuation.

	TIC 201739321	_TIC 255996252_	_TIC 312637783_	_TIC 317512446_	_TIC 335484421_	_TIC 354793407_
⁶ C		8.19 ± 0.35 (13)	8.39 ± 0.32 (29)	8.94 ± 0.27 (7)	8.78 ± 0.41 (6)	
⁷ N		7.45 ± 0.24 (2)	7.87 ± 0.36 (21)	8.03 ± 0.28 (1)		
⁸ O		8.79 ± 0.24 (2)				
¹¹ Na		6.50 ± 0.26 (2)			6.44 ± 0.46 (2)	
¹² Mg	7.72 ± 0.24 (5)	7.65 ± 0.34 (7)	8.58 ± 0.46 (1)	8.10 ± 0.30 (8)	7.71 ± 0.39 (4)	7.64 ± 0.35 (3)
¹⁴ Si	7.29 ± 0.31 (2)	7.49 ± 0.23 (10)	7.64 ± 0.44 (7)	7.33 ± 0.26 (6)	7.40 ± 0.26 (12)	8.19 ± 0.25 (15)
¹⁶ S		7.65 ± 0.24 (2)	7.01 ± 0.43 (8)	7.50 ± 0.36 (2)	6.72 ± 0.34 (9)	
²⁰ Ca	6.22 ± 0.30 (7)	6.75 ± 0.32 (10)		6.81 ± 0.27 (13)	6.66 ± 0.32 (23)	6.15 ± 0.41 (3)
²¹ Sc	2.84 ± 0.32 (4)	3.57 ± 0.32 (7)		3.59 ± 0.34(3)	3.69 ± 0.36 (4)	
²² Ti	4.73 ± 0.29 (12)	5.17 ± 0.39 (25)		5.47 ± 0.35 (36)	5.08 ± 0.34 (35)	6.47 ± 0.39 (4)
²³ V		4.36 ± 0.38 (5)		4.43 ± 0.39 (2)	5.09 ± 0.38 (4)	5.29 ± 0.39 (1)
²⁴ Cr	5.53 ± 0.26 (10)	5.82 ± 0.33 (22)		5.97 ± 0.29 (22)	5.93 ± 0.23 (35)	6.75 ± 0.30 (13)
²⁵ Mn	5.05 ± 0.31 (1)	5.51 ± 0.24 (2)		5.53 ± 0.37 (2)	5.68 ± 0.36 (11)	6.55 ± 0.32 (2)
²⁶ Fe	7.26 ± 0.25 (23)	7.61 ± 0.30 (75)	7.46 ± 0.43 (26)	7.79 ± 0.22 (98)	7.77 ± 0.26 (116)	8.19 ± 0.26 (88)
²⁷ Co					5.98 ± 0.48 (1)	
²⁸ Ni	6.14 ± 0.33 (2)	6.38 ± 0.39 (19)	7.23 ± 0.46 (2)	6.60 ± 0.32 (6)	6.78 ± 0.30 (31)	7.00 ± 0.35 (8)
²⁹ Cu					3.93 ± 0.46 (1)	
³⁰ Zn					4.72 ± 0.46 (1)	
³⁸ Sr		3.71 ± 0.24 (1)		4.17 ± 0.33 (1)	4.22 ± 0.36 (2)	
³⁹ Y		2.79 ± 0.31 (5)		2.80 ± 0.38 (1)	3.01 ± 0.35 (3)	
⁴⁰ Zr		3.14 ± 0.36 (1)	3.34 ± 0.29 (3)		3.92 ± 0.37 (1)	3.48 ± 0.39 (3)
⁵⁶ Ba			3.18 ± 0.24 (2)		2.64 ± 0.38 (2)	3.74 ± 0.42 (2)

Table A2. Continuation.

	.TIC 367351021.	TIC 374038418	.TIC 377099704.	.TIC 377443211.	.TIC 387757610.	.TIC 467219052.
Element	Abundance	Abundance	Abundance	Abundance	Abundance	Abundance
⁶ C	8.38 ± 0.136 (13)		8.31 ± 0.28 (12)		8.30 ± 0.37 (6)	8.31 ± 0.46 (5)
⁷ N	8.15 ± 0.26 (1)		8.09 ± 0.30 (12)			
⁸ O	8.96 ± 0.26 (2)			8.90 ± 0.35 (2)	8.73 ± 0.28 (4)	8.83 ± 0.30 (1)
¹¹ Na	6.72 ± 0.26 (2)				6.83 ± 0.37 (2)	6.36 ± 0.30 (1)
¹² Mg	8.03 ± 0.33 (5)	7.43 ± 0.56 (1)	8.32 ± 0.37 (5)	7.90 ± 0.36 (5)	7.99 ± 0.33 (5)	7.73 ± 0.38 (3)
¹⁴ Si	7.64 ± 0.43 (17)		7.01 ± 0.31 (18)	8.05 ± 0.31 (3)	7.46 ± 0.40 (6)	7.36 ± 0.30 (5)
¹⁶ S	7.44 ± 0.26 (2)				8.26 ± 0.34 (2)	7.06 ± 0.30 (1)
²⁰ Ca	6.58 ± 0.32 (15)	6.96 ± 0.57 (1)		6.31 ± 0.31 (5)	6.42 ± 0.33 (7)	6.36 ± 0.38 (12)
²¹ Sc	3.23 ± 0.28 (7)			2.91 ± 0.34 (2)	2.99 ± 0.30 (4)	3.22 ± 0.26 (5)
²² Ti	5.12 ± 0.32 (23)			5.02 ± 0.37 (6)	5.15 ± 0.36 (10)	5.23 ± 0.39 (12)
²³ V						4.19 ± 0.30 (1)
²⁴ Cr	5.80 ± 0.40 (21)			5.66 ± 0.32 (6)	5.60 ± 0.34 (9)	5.82 ± 0.34 (10)
²⁵ Mn	5.55 ± 0.25 (3)				5.35 ± 0.34 (2)	
²⁶ Fe	7.54 ± 0.30 (86)	8.53 ± 0.46 (2)	7.31 ± 0.31 (19)	7.31 ± 0.30 (30)	7.40 ± 0.36 (18)	7.49 ± 0.30 (40)
²⁷ Co						
²⁸ Ni	6.34 ± 0.39 (29)	7.47 ± 0.48 (1)			6.28 ± 0.33 (5)	6.20 ± 0.30 (8)
²⁹ Cu						
³⁰ Zn	5.92 ± 0.34 (1)					4.99 ± 0.30 (1)
³⁸ Sr					3.41 ± 0.34 (1)	2.76 ± 0.30 (1)
³⁹ Y	2.51 ± 0.34 (2)				3.13 ± 0.33 (2)	2.41 ± 0.30 (1)
⁴⁰ Zr						3.10 ± 0.30 (1)
⁵⁶ Ba	2.59 ± 0.32 (3)			1.90 ± 0.34 (2)	2.55 ± 0.33 (2)	2.48 ± 0.31 (3)